Nucleation, Growth, and Agglomeration in Barium Sulfate Turbulent Precipitation

Daniele L. Marchisio, Antonello A. Barresi, and Mirko Garbero
Dip. Scienza dei Materiali ed Ingegneria Chimica, Politecnico di Torino, 10129, Torino, Italy

In this work barium sulfate precipitation is studied in a tubular reactor in a wide range of operating conditions. The effect of reactant concentrations and barium or sulfate excess on crystal-size distribution and morphology is investigated. Experimental results show that ion excess has a strong influence and that at high concentration aggregation takes place. Computational fluid dynamics is coupled with the finite-mode probability density function approach for taking into account both macro- and micromixing, whereas the population balance is treated by using the standard moment method. Comparison with experimental data suggests that when micromixing and agglomeration are properly taken into account, the agreement is improved. However, this statement is partially affected by the lack of knowledge in barium sulfate kinetics.

Introduction

Many chemical processes, such as catalysts, pigments and pharmaceutical products preparation, offshore oil drilling, and water treatment, involve precipitation in one or more key steps of the overall operation. Precipitation is a very complex problem, since it is influenced by several interacting phenomena, and for this reason has attracted much attention.

Precipitation occurs through several steps, namely nucleation, crystal growth, and eventually aggregation and breakup. Since the process is fast, mixing at various scales plays a crucial role in determining the final crystal-size distribution (CSD) and crystal morphology. Several test precipitation reactions have been used for investigation: calcium carbonate, barium sulfate, calcium oxalate, yttrium oxalate. A number of works have been published in this field, trying to explain different aspects of the process.

Sung et al. (2000) investigated the yttrium oxalate precipitation in a semibatch reactor, focusing on the competition between aggregation and breakage. The role of solution composition was studied by Bramley et al. (1997), leading to the conclusion that ionic strength influence on the electrical double layer of each crystal is not able alone to explain the final effect on aggregation rate. The effect of ion excess on barium sulfate precipitation has been recently studied (Wong et al., 2001), and results show that it has a strong influence on crystal growth and nucleation. Zauner and Jones (2000) derived kinetic expressions for nucleation, growth, aggregation, and breakage from experimental precipitation data for the calcium oxalate system, by using a novel approach based on the separate extraction of kinetic rates from the CSD.

Baldyga's group focused on the influence of mixing on the reaction course (Baldyga et al., 1995) and on the modeling approach (Baldyga and Orciuch, 1997). In this last work the authors proposed a presumed probability density function (PDF) method (based on beta-PDF) coupled with computational fluid dynamics (CFD). The population balance was solved by using the standard moment methods (SMM) neglecting aggregation. In another work (Marchisio et al., 2001a), a finite-mode PDF (FM-PDF) method was coupled with CFD for studying barium sulfate precipitation in a semibatch Taylor-Couette reactor. An alternative to the SMM is the classic discretized population balance (DPB) approach, in which the internal coordinate is discretized, and the population balance is transformed in a set of ordinary differential equations (for homogeneous flow). Several methods have been proposed (Hounslow et al., 1988; Litster et al., 1995) for handling simultaneous nucleation, aggregation, and growth. Use of these methods requires a large number of scalars to be solved, and in the case of implementation in a CFD code, for complex (2-D or 3-D) geometry, could result in an elevated computational time. Starting from the idea of the SMM, McGraw (1997) proposed the use of the quadrature method of moments (QMOM) for size-dependent growth rate, but it has not been employed for aggregation applications yet.

Correspondence concerning this article should be addressed to A. A. Barresi.
Current address of D. L. Marchisio: Dept. of Chemical Engineering, Iowa State University, 3131 Sweeney Hall, Ames, IA 50011.

The aim of this work is to study barium sulfate precipitation in a single-jet tubular reactor. The effect of ion excess and reactant concentrations on CSD and morphology was investigated in a wide range of operating conditions. Measurements were carried out with an on-line measurement system for gathering information on CSD in the early stage of precipitation. Moreover, samples taken from the reactor outlet were monitored in order to determine the advancement of the reaction. A scanning electron microscope (SEM) was used to investigate crystal morphology and to calculate crystal-shape factors. Experimental data were compared with model predictions obtained by using a CFD code coupled with a FM-PDF model for micromixing and the SMM approach for the population balance.

Precipitation Model

Precipitation modeling requires an adequate description of mixing, population balance, and has to be based on appropriate kinetic expressions. In what follows all these aspects will be presented and cleared.

Micromixing model

The tubular reactor is modeled by using CFD. In this approach macro- and mesomixing are described by the Reynolds-average Navier–Stokes (RANS) equations, modeling convection, and turbulent diffusion, whereas micromixing is taken into account by introducing a sub-grid-scale micromixing model. A detailed description of the model can be found in Marchisio et al. (2001a) and Piton et al. (2000), and only a brief summary is given in the following. Using this approach the composition PDF is represented by a finite set of delta functions (Fox, 1998)

$$f_\phi(\psi;\boldsymbol{x},t) \equiv \sum_{n=1}^{N_e} p_n(\boldsymbol{x},t)\prod_{\alpha=1}^{m}\delta\left(\psi_\alpha-\langle\phi_\alpha\rangle_n(\boldsymbol{x},t)\right) \tag{1}$$

where $f_\phi(\psi;\boldsymbol{x},t)$ is the joint PDF of all scalars (for example, concentrations, moments) appearing in the precipitation model, $p_n(\boldsymbol{x},t)$ is the probability of mode n, $\langle\phi_\alpha\rangle_n(\boldsymbol{x},t)$ is the value of scalar α corresponding to mode n, N_e is the total number of modes, and m is the total number of scalars.

The effect of N_e has been extensively studied in Marchisio (2002). Model performances for $N_e=1$ (neglecting micromixing) and $N_e=2$, 3, 4, have been investigated and compared. The results showed that $N_e=3$ is an acceptable trade-off between accuracy and computational time. The evolution of these mode probabilities will be defined once a transport equation for the probability vector $p_n(\boldsymbol{x},t)$ is provided

$$\frac{\partial p_1}{\partial t}+\frac{\partial}{\partial x_i}\left(\langle u_i\rangle p_1\right)=\frac{\partial}{\partial x_i}\left(\Gamma_t\frac{\partial p_1}{\partial x_i}\right)+\gamma_s p_3-\gamma p_1(1-p_1) \tag{2}$$

$$\frac{\partial p_2}{\partial t}+\frac{\partial}{\partial x_i}\left(\langle u_i\rangle p_2\right)=\frac{\partial}{\partial x_i}\left(\Gamma_t\frac{\partial p_2}{\partial x_i}\right)+\gamma_s p_3-\gamma p_2(1-p_2) \tag{3}$$

where $p_3=1-p_1-p_2$, Γ_t is the turbulent diffusivity, γ is the molecular mixing rate, whereas γ_s is the "spurious" scalar dissipation rate resulting from the finite-mode representation.

This approach can be thought of as a discretization of every cell of the computational domain in three modes. Fluid enters the computational domain through modes 1 and 2, while mode 3 corresponds to the partially mixed reacting fluid. We will take the first scalar to be the mixture fraction, defined in terms of a local value $[\langle\xi\rangle_n]$ in mode n and weighted value $[\langle s_\xi\rangle_n=\langle\xi\rangle_n p_n]$. In order to ensure mass conservation, transport equations are written in terms of weighted concentrations. For the weighted mixture fraction this equation is

$$\frac{\partial\langle s_\xi\rangle_3}{\partial t}+\frac{\partial}{\partial x_i}\left(\langle u_i\rangle\langle s_\xi\rangle_3\right)=\frac{\partial}{\partial x_i}\left(\Gamma_t\frac{\partial\langle s_\xi\rangle_3}{\partial x_i}\right)-\gamma_s p_3(\langle\xi\rangle_1+\langle\xi\rangle_2)+\gamma p_1(1-p_1)\langle\xi\rangle_1+\gamma p_2(1-p_2)\langle\xi\rangle_2 \tag{4}$$

with $p_1=1$, $p_2=0$, $\langle s_\xi\rangle_3=0$ and $p_1=0$, $p_2=1$, $\langle s_\xi\rangle_3=0$ as boundary conditions in the two inlet streams.

Then, by forcing the mean mixture fraction $\langle\xi\rangle$ and the mixture fraction variance $\langle\xi'^2\rangle$ to agree with their transport equations, γ and γ_s were shown to be as follows

$$\gamma=C_\phi\frac{\epsilon}{k}\frac{\langle\xi'^2\rangle}{\left[p_1(1-p_1)(1-\langle\xi\rangle_3)^2+p_2(1-p_2)\langle\xi\rangle_3^2\right]} \tag{5}$$

$$\gamma_s=\frac{2\Gamma_t}{1-2\langle\xi\rangle_3(1-\langle\xi\rangle_3)}\frac{\partial\langle\xi\rangle_3}{\partial x_i}\frac{\partial\langle\xi\rangle_3}{\partial x_i} \tag{6}$$

where k is the turbulent kinetic energy, ϵ is the turbulent dissipation rate, and C_ϕ is a constant of the order of magnitude of unity. In the case of finite-rate chemical reactions the relationships between concentrations, mixture fraction, and reaction progress variable (Y) are

$$\frac{c_A}{c_{Ao}}=\xi-\xi_s Y,\qquad \frac{c_B}{c_{Bo}}=(1-\xi)-(1-\xi_s)Y \tag{7}$$

where

$$\xi_s=\frac{c_{Bo}}{c_{Ao}+c_{Bo}} \tag{8}$$

Eventually a transport equation for the weighted reaction progress variable $\langle s_Y\rangle_3$ must be added

$$\frac{\partial\langle s_Y\rangle_3}{\partial t}+\frac{\partial}{\partial x_i}\left(\langle u_i\rangle\langle s_Y\rangle_3\right)=\frac{\partial}{\partial x_i}\left(\Gamma_t\frac{\partial\langle s_Y\rangle_3}{\partial x_i}\right)+\frac{p_3 S(\langle c_A\rangle_3,\langle c_B\rangle_3)}{\xi_s c_{Ao}} \tag{9}$$

where $S(\langle c_A\rangle_3,\langle c_B\rangle_3)$ is the source term for the chemical reaction, and $\langle c_A\rangle_3$ and $\langle c_B\rangle_3$ are calculated from Eq. 7 using $\langle\xi\rangle_3=\langle s_\xi\rangle_3/p_3$ and $\langle Y\rangle_3=\langle s_Y\rangle_3/p_3$.

Population balance

The population balance is a continuity statement expressed in terms of the particle number density function [$n(L;\ \boldsymbol{x},\ t)$] with the length as the internal coordinate (Randolph and Larson, 1988)

$$\frac{\partial n(L;\ \boldsymbol{x},\ t)}{\partial t}+\frac{\partial}{\partial x_i}\left[\langle u_i\rangle n(L;\ \boldsymbol{x},\ t)\right]=\frac{\partial}{\partial x_i}\left(\Gamma_t\frac{\partial n(L;\ \boldsymbol{x},\ t)}{\partial x_i}\right)$$

$$+\frac{\partial}{\partial L}\left[G(L)n(L;\ \boldsymbol{x},\ t)\right]+B(L;\ \boldsymbol{x},\ t)-D(L;\ \boldsymbol{x},\ t) \quad (10)$$

where L is the crystal dimension, $G(L)$ is the growth rate, and $B(L)$ and $D(L)$ are, respectively, the birth and the death rates due to aggregation, which can be expressed as follows (Hounslow et al., 1988)

$$B(L)=\frac{L^2}{2}\int_0^L\frac{\beta\left[(L^3-\lambda^3)^{1/3},\ \lambda\right]n\left[(L^3-\lambda^3)^{1/3}\right]n(\lambda)\ d\lambda}{(L^3-\lambda^3)^{2/3}} \quad (11)$$

$$D(L)=n(L)\int_0^\infty\beta(L,\ \lambda)n(\lambda)\ d\lambda \quad (12)$$

where L and λ are particle dimensions, and β is the aggregation kernel, which is a measure of the frequency of collision of the particles that are successful in producing a new particle. Notice that Eq. 10 is written neglecting fluctuations.

Since reaction and particle formation occur only in mode 3, the population balance in terms of the moments has to be solved only for this mode. In the case of size-independent growth rate, the final set of equations for the first five moments is as follows

$$\frac{\partial\langle s_{m_k}\rangle_3}{\partial t}+\frac{\partial}{\partial x_i}\left(\langle u_i\rangle\langle s_{m_k}\rangle_3\right)=\frac{\partial}{\partial x_i}\left(\Gamma_t\frac{\partial\langle s_{m_k}\rangle_3}{\partial x_i}\right)$$

$$+(0)^k p_3 J\left(\langle c_A\rangle_3,\langle c_B\rangle_3\right)+kG\left(\langle c_A\rangle_3,\langle c_B\rangle_3\right)\langle s_{m_{k-1}}\rangle_3$$

$$+p_3\left(\overline{B_k}-\overline{D_k}\right) \quad (13)$$

with $k=0,\ \ldots,\ 4$, and where $J(\langle c_A\rangle_3,\ \langle c_B\rangle_3)$ is the nucleation rate in mode 3, $\langle s_{m_k}\rangle_3$ is the weighted kth moment and $\overline{B_k}$ is

$$\overline{B_k}=\frac{\beta_0}{2}\int_0^\infty\langle n(\lambda)\rangle_3\int_0^\infty(u^3+\lambda^3)^{k/3}\langle n(u)\rangle_3\ du\ d\lambda \quad (14)$$

where $u^3=L^3-\lambda^3$, and $\overline{D_k}$ is

$$\overline{D_k}=\beta_0\int_0^\infty\langle n(L)\rangle_3 L^k\int_0^\infty\langle n(\lambda)\rangle_3\ d\lambda\ dL \quad (15)$$

where $\langle n(L)\rangle_3$ is the local particle number density function in mode 3, and the aggregation kernel is assumed to be constant [$\beta(L,\ \lambda)\approx\beta_0$]. The problem is closed if $\overline{B_k}$ and $\overline{D_k}$ are expressed in terms of the moments of the CSD. As explained in Marchisio et al. (2000), in the case of constant kernel, and after some simplifications, $\overline{B_k}$ and $\overline{D_k}$ become

$$\overline{B_k}=\beta_0 b_k\langle m_0\rangle_3\langle m_k\rangle_3 \quad (16)$$

$$\overline{D_k}=\beta_0\langle m_0\rangle_3\langle m_k\rangle_3 \quad (17)$$

where $\langle m_k\rangle_3$ is the local kth moment [$\langle m_k\rangle_3=\langle s_{m_k}\rangle_3/p_3$] and b_k are found by solving Eq. 14. Notice that $b_0=1/2$ and $b_3=1$ are derived from the exact solution of the integral in Eq. 14, whereas $b_1=2/3$, $b_2=5/6$, and $b_4=7/6$ are derived by replacing $(u^3+\lambda^3)^{k/3}$ with its Taylor series. This approach presents several limitations, and a detailed discussion can be found in Marchisio et al. (2000). However, it is possible to say that in the case of constant kernel and under limited aggregation rates the errors are acceptable.

Using this approach the mean crystal size can be written as follows

$$L_{43}=\frac{m_4}{m_3} \quad (18)$$

and the solid concentration is given by

$$c_C=\frac{\rho k_v m_3}{M} \quad (19)$$

where ρ is the crystal density, k_v is the volume shape factor, M is the molecular weight of the crystal. Concerning the chemical source term, it can be written as follows

$$p_3 S\left(\langle c_A\rangle_3,\langle c_B\rangle_3\right)=\frac{\rho k_a\langle s_{m_2}\rangle_3}{2M}G\left(\langle c_A\rangle_3,\langle c_B\rangle_3\right) \quad (20)$$

where k_a is the area shape factor that will be defined in the next section.

Precipitation kinetics

As mentioned in the Introduction, precipitation involves different steps: nucleation, crystal growth, aggregation, and breakage. A detailed review of all these processes can be found in Dirksen and Ring (1991). During precipitation, new particles, called nuclei, are created by nucleation events. The nucleation process can be broken into two main categories: (1) primary homogeneous nucleation, and (2) primary heterogeneous nucleation. Homogeneous nucleation occurs in the absence of a solid interface, while heterogeneous nucleation occurs in the presence of a solid interface. Using Nielsen's experimental data of barium sulfate precipitation (Nielsen, 1964), Baldyga and coworkers (Baldyga et al., 1995) found an

expression for the nucleation rate

$$J(c_A, c_B) = \begin{cases} 2.83\times10^{10}\Delta c^{1.775}\ \left(1/\mathrm{m}^3\cdot\mathrm{s}\right) & \text{for } \Delta c \le 10\ \mathrm{mol/m}^3\ \text{(heterogeneous)} \\ 2.53\times10^{-3}\Delta c^{15}\ \left(1/\mathrm{m}^3\cdot\mathrm{s}\right) & \text{for } \Delta c > 10\ \mathrm{mol/m}^3\ \text{(homogeneous)} \end{cases} \tag{21}$$

where $\Delta c = \sqrt{c_A c_B} - \sqrt{k_s}$, c_A, c_B are reactant concentrations, and k_s is the solubility product of barium sulfate (at room temperature $k_s = 1.14\times10^{-4}$ mol^2/m^6). This expression does not account for ion excess, which on the contrary was shown to have an effect on the final CSD (Wong et al., 2001; Phillips et al., 1999). A detailed study of the effect of this ion excess on kinetics, and a review of a number of kinetic expressions available in the literature was done by Aoun et al. (1996, 1999). Unfortunately their expressions were derived in a relatively small range of reactant concentration, and, thus, they are not applicable to this study.

Concerning crystal growth, several processes are involved, such as diffusion of solute from the solution bulk to crystal surface, adsorption on crystal surface, diffusion over the surface, attachment to a step, diffusion along a step, and integration into a crystal kink site. As explained by Dirksen and Ring (1991) and Nielsen (1984), different growth laws can be obtained, linear, parabolic, and exponential, if the controlling mechanism is, respectively, diffusion, surface spiral growth, and surface nucleation (polynuclear). Concerning barium sulfate growth rate, Nielsen and Toft (1984), by fitting experimental data, proposed a parabolic expression with a kinetic constant (k_r) equal to 5.8×10^{-8} (m/s)/(mol/m^3)^2. In normal applications, barium sulfate growth is controlled not only by surface growth but also by diffusion. The final growth rate can be found as follows

$$G(c_A, c_B) = 5.8\times10^{-8}\Delta c_s^2 = k_d(c_A - c_{As}) = k_d(c_B - c_{Bs})\ (m/s) \tag{22}$$

where $\Delta c_s = \sqrt{c_{As}c_{Bs}} - \sqrt{k_s}$, c_{As} and c_{Bs} are reactant concentrations on the crystal surface, and k_d is the mass-transfer coefficient. The solution of this equation for given values of c_A and c_B (bulk concentration) can be found by using a simple Newton–Raphson method. Dirksen and Ring (1991) showed that for particles smaller than 1 μm the slip velocity is very small and then particles are entrapped in a microeddy. In this condition the growth rate is typically controlled by Brownian diffusion and higher growth rates for sparingly soluble species are observed. Armenante and Kirwan (1989) derived a relationship for the Sherwood number

$$Sh = 2 + 0.52\,Re^{0.52}Sc^{1/3} \tag{23}$$

where Re and Sc are the Reynolds and Schmidt numbers, respectively. This study is the first systematic experimental confirmation that the theoretical limit of Sherwood number equal to 2 is valid for spherical particles in agitated systems. Using this expression in the limit of null slip velocity, we find that

$$k_d = \frac{ShDM}{L_{43}\rho} \approx \frac{2.0\times10^{-13}}{L_{43}} \tag{24}$$

where D is the molecular diffusion coefficient, M is the molecular weight, ρ is the crystal density, and L_{43} is used as an equivalent particle dimension. According to this equation, k_d increases with decreasing particle dimension. A different result was obtained by Nagata (1975), who reported constant k_d for particles smaller than 10 μm notwithstanding the difference in solute. The use of a size-dependent growth rate (by using Eq. 22 coupled with Eq. 24) seems to be more theoretically based, and it must be mentioned that a limited number of experimental data was used by Nagata to achieve his conclusion. In spite of this, a constant k_d was considered in this work, due to computational constraints, as discussed in the next section.

Wei and Garside (1997), by using the expression provided by Bromley (1973), included activity coefficients in kinetic expressions in order to include nonideal effects of ions. However, the use of activity coefficients seems to be questionable, since this kind of treatment is usually used for determining equilibrium conditions and not for kinetic expressions that are expressed in terms of concentrations, and in any case, is not effective in describing the influence of ion excess on CSD (Marchisio et al., 2001b).

Concerning aggregation kinetics, collision is caused by fluid motion and Brownian motion. Depending on the type of flow (laminar or turbulent) of the media, different expressions for the aggregation kernel were found (Smoluchowski, 1917; Saffman and Turner, 1956)

$$\beta(L, \lambda) = \begin{cases} \dfrac{4}{3}\gamma_l(L+\lambda)^3 & \text{laminar flow} \\ \left(\dfrac{8\pi}{15}\right)^{1/2}\left(\dfrac{\epsilon}{\nu}\right)^{1/2}(L+\lambda)^3 & \text{turbulent flow} \end{cases} \tag{25}$$

where γ_l is the laminar shear stress and ν is the kinematic viscosity. In case of particle collision due to Brownian motion, the aggregation kernel is as follows (Smoluchowski, 1917)

$$\beta(L, \lambda) = \frac{2k_BT}{3\mu}\frac{(L+\lambda)^2}{L\lambda} \tag{26}$$

where k_B is the Boltzmann constant, T is the absolute temperature, and μ is the kinematic viscosity. If the colliding particles are of about the same size ($L \approx \lambda$), the kernel can be assumed constant

$$\beta_0 = \frac{8k_BT}{3\mu} = 10^{-17}\ m^3/s \tag{27}$$

Concerning shape factors, experimental evidence showed that by using a laser particle sizer, when crystals are flat the crys-

tal size detected by the instrument (d_{43}) is approximately the width of the crystal (Pagliolico et al., 1999), whereas when crystals are round-shaped, it is approximately the diameter of the sphere that includes the crystal. If d_{43} is chosen as the characteristic dimension, real shape factors (K_a, K_v) are defined as follows

$$V = K_v d_{43}^3 \tag{28}$$

$$A = K_a d_{43}^2 \tag{29}$$

Generally K_a/K_v is not equal to 6, which is the characteristic value for a system with equidimensional growth. Since the population balance is written with only one internal coordinate (that is, L_{43}) that is intermediate between the dimensions of the crystal along each crystal axis, average shape factors (k_a, k_v) have to be recalculated in terms of L_{43}

$$V = K_v d_{43}^3 = k_v L_{43}^3 \tag{30}$$

$$A = K_a d_{43}^2 = k_a L_{43}^2 \tag{31}$$

imposing equidimensional growth

$$k_a/k_v = 6 \tag{32}$$

New shape factors are obtained with this approach, and the relationship between real and characteristic crystal size can be written as

$$d_{43} = \phi_c L_{43} \tag{33}$$

where ϕ_c is derived by solving Eqs. 30–32.

Experimental Setup

Barium sulfate precipitation was carried out in a tubular reactor with a single-jet configuration. The tubular reactor is 2.1 m long and has an internal diameter of 1 cm. The jet is positioned on the reactor axis, and is made of a small pipe (ID = 1 mm and OD = 1.5 mm). The two reactants were separately fed in the small tube and in the annular region. Distilled water and analytical grade reagents were used to prepare barium chloride and sodium sulfate solutions.

Two different series of measurements were performed: on- and off-line. In the first ones the reactor outlet was connected with the laser particle sizer (Coulter LS 230), as reported in Figure 1, and the CSD was directly measured on the particles flowing in the outlet fluid. In this case, the laser particle sizer was used with the "fluid cell" device. These experiments were carried out because in certain cases the reaction was not complete and would have progressed during sampling and analysis. On-line measurements were complicated by particle deposition over the cell lens. In order to minimize particle deposition the measurement time was reduced from 60 to 15 s and after each run all the lines, including piping, tubular reactor, and particle sizer, were cleaned with washing water and the particle sizer cell was mechanically cleaned.

In spite of all the precautions to avoid particle deposition, deposited particles were found on the optical lens after each run. The main point was to verify if the amount of deposited particles was adding further appreciable scattering, and, thus, altering measurements. After cleaning the line with distilled water another measurement was carried out. In the complete absence of particle deposition, this would result in a blank test, with particle deposition resulting in the CSD of deposited particles. In several runs the amount of deposition was so small that the instrument did not detect it, and when it was detected results showed that there was a small overlap between the CSDs of flowing and deposited particles. In these experiments the data scatter was relatively high, especially in the two sets of runs at lower concentrations; for these cases the experiments were repeated 5–6 times.

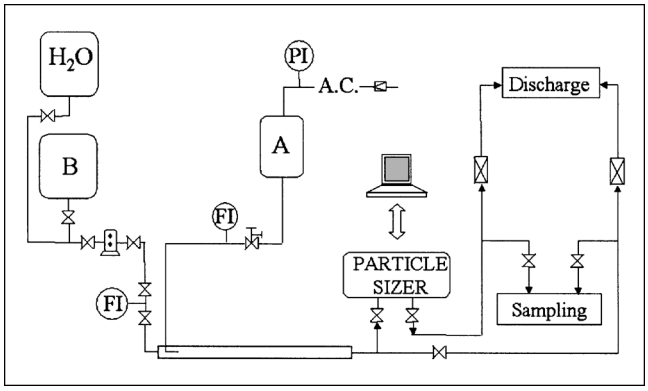

Figure 1. Experimental setup.

In the off-line measurements samples from the reactor outlet were taken and gently stirred. The CSD was measured by using the particle sizer with the "small volume cell," at different time increments. Samples taken at the reactor outlet were filtered and simultaneously diluted in order to avoid further growth. Filtered particles were dried in a stove at 120°C, and after redispersion in acetone, prepared for SEM observation.

Operating Conditions

The inlet velocity in the annular region was kept equal to 1 m/s, because of on-line measurement constraints, so that the macroscopic Reynolds number was equal to 10,000. This Reynolds number is well above turbulent transition, but is lower than in other works in the literature (Baldyga and Orciuch, 1997). Generally the Reynolds number is kept at higher values to ensure a fully developed turbulent flow, since only in this condition are turbulence models and turbulent mixing models applicable. This requirement was irreconcilable with on-line measurements. In fact, the residence time of the particles in the particle sizer cell decreases with increasing *Re*, and under a certain value measurement was not possible. However, given the number of works that have been published under these operating conditions (Li and Toor, 1986; Pipino and Fox, 1994), and the great advantage of observing precipitation in its early stages, this Reynolds number value (10,000) was considered an acceptable trade-off between turbulence intensity and measurement accuracy. All the experiments were carried out with the ratio between the velocity in the feed stream in the nozzle and the feed stream in the annular region (VR) equal to one. Barium chloride was fed

Table 1. Operating Conditions of Experiments*

Reactant Fed in the Inner Tube			
$\alpha = c_{Bo}/c_{Ao}$	$BaCl_2$ $c_{Ao} = 34$ mol/m^3	Na_2SO_4 $c_{Ao} = 34$ mol/m^3	$BaCl_2$ $c_{Ao} = 341$ mol/m^3
0.01	OT	OT	OT
0.10	OTM	OT	OTM
1.00	OTM	OT	OTM
1.50	OTM	OT	T
3.00	OTM	OTM	T

*The second column refers to case 1; the third column to case 2; and the fourth column to case 3.
Key: O on-line measurements; T off-line measurements; M SEM observation.

either in the nozzle or in the annular region while sodium sulfate was fed in the other region. Initial reactant concentrations (c_{Ao}, c_{Bo}) used in the experiments are reported in Table 1 with the relative measurements carried out.

The second column (case 1) refers to experiments carried out at a low concentration level with barium chloride in the nozzle and sodium sulfate in the annular flow. Concentration of the reactant fed in the nozzle (barium chloride, in this case) was the same in all the runs of this series, whereas the concentration of the reactant fed in the annular region was varied in order to keep the ratio between the two concentrations ($\alpha = c_{Bo}/c_{Ao}$) between 0.1 and 3. Notice that, as the ratio of the two feed stream rates (Q_{Bo}/Q_{Ao}) is equal to 100, the condition for $\alpha = 0.01$ yields equal concentrations after complete mixing without reaction ($c_{Ao}Q_{Ao} = c_{Bo}Q_{Bo}$), keeping the stoichiometric ratio.

The feed positions were inverted and then sodium sulfate was fed in the nozzle and barium chloride was fed in the annular region, keeping the overall concentration level at the same values (third column, case 2). Moreover, because at these initial reactant concentrations the final solid concentration was too low to have extended aggregation, keeping the configuration experiments in the first column basic, concentrations were increased by a factor of 10. Then experiments at high concentration (fourth column, case 3) were carried out with barium chloride in the nozzle and sodium sulfate in the annular flow.

Computational Details

Simulations were carried out by using a commercial CFD code (Fluent 5.2). The real 3-D geometry was modeled under the hypothesis of axialsymmetry. Figure 2 shows the tubular reactor and the computational domain. Different grids were tested in order to find a grid-independent solution, and the final grid was with 131 nodes in the axial direction and 35 nodes in the radial direction. The standard $\kappa - \epsilon$ model with standard wall functions was used. The micromixing model and the population balance were introduced via user-defined functions.

The complete model is constituted by a set of nine transport equations, in which the convection and the turbulent diffusion are modeled by the CFD code, and a source term must be specified for each scalar. This was done by means of user-defined subroutines. After solving the flow field, once mean velocities and turbulence quantities were known, mixing properties were determined by solving the transport equations for p_1, p_2, and $\langle s_\xi \rangle_3$ according to Eqs. 2–4. Then reaction and particle formation were solved for mode 3 by solving the transport equations for the reaction progress variable [$\langle s_Y \rangle_3$], and for the moments of the CSD ($\langle s_{m_k} \rangle_3$ with $k = 0, \ldots, 4$], according to Eqs. 9 and 13.

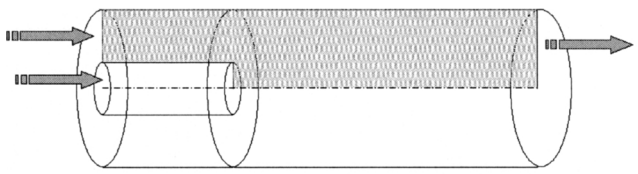

Figure 2. Computational domain used in the simulations.

Simulations were carried out by using Eq. 21 for nucleation rate and Eq. 22 for growth rate. Since it is not possible to consider a size-dependent growth rate (that is, to employ Eq. 24 for estimating the mass-transfer coefficient) if the SMM is used to solve the population balance, k_d was considered as a psuedoconstant parameter. Concerning the choice of its value, in a previous work (Marchisio et al., 2001c) it was found that under these operating conditions the best-fit value for k_d is 10^{-6} (m/s)/(mol/m^3), and this specific value was used in this work.

Shape factors were determined from an experimental observation of crystal morphology, as will become clearer in the following sections.

Two inlet streams were defined into the computational domain. For the first one (jet stream), $p_1 = 1$ and $p_2 = 0$, while for the second one (annular region), $p_1 = 0$ and $p_2 = 1$. All the other variables were set equal to zero in the two inlet streams. Underrelaxation factors were used for the flow-field default, whereas for user-defined scalars variable factors were used, depending on the stiffness of the problem. Generally for low reactant concentrations unitary factors were used, while for increasing concentrations underrelaxation factors were reduced down to 0.6. Convergence was considered reached when all the normalized residuals were lower than 10^{-6}.

Simulations were carried out for cases 1 and 2 and for case 3. Since the model is perfectly symmetric, experimental cases 1 and 2 correspond to a unique series of simulations; experimental case 3 corresponds to another series of simulations. Model predictions were compared with experimental data with and without the micromixing model and with and without the aggregation terms in the population balance, to assess the contribution of these phenomena.

Results and Discussion

The effect of the concentration ratio ($\alpha = c_{Bo}/c_{Ao}$) on CSD and crystal morphology was investigated for the different cases (see Table 1). First we investigated the variation with time of the mean crystal size in the suspension sampled at the reactor outlet, in order to find how complete the reaction is and the number of crystals formed.

In Figure 3 the mean crystal-size evolution vs. time for values of α in case 1 ($BaCl_2$ in the nozzle) is reported. Notice that as explained before, $\alpha = 0.01$ corresponds to the final reactant concentration ratio after complete mixing without

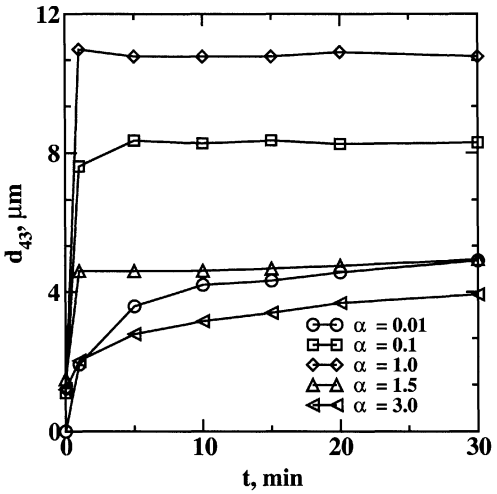

Figure 3. Time evolution of mean crystal size (d_{43}) in sampled suspensions as a function of the concentration ratio (α).

$BaCl_2$ fed in the nozzle, $c_{Ao} = 34$ mol/m^3. The first point represents the tubular reactor outlet.

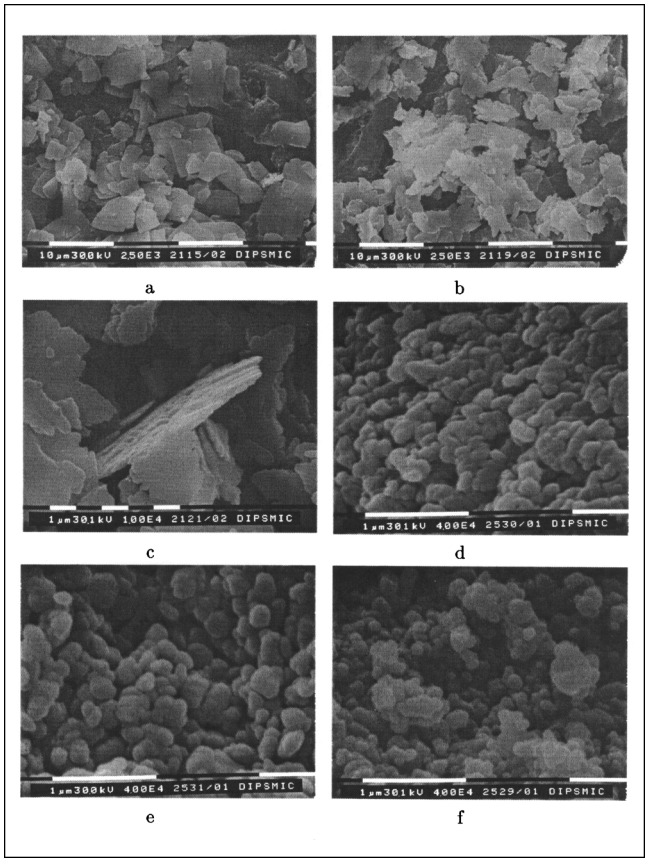

Figure 4. Crystal morphologies.

(a) Tabular crystals ($BaCl_2$ in the jet $c_{Ao} = 34$ mol/m^3, $\alpha = 0.1$); (b) dendritic crystals ($BaCl_2$ in the jet $c_{Ao} = 34$ mol/m^3, $\alpha = 1.0$); (c) particular of a dendritic crystal ($BaCl_2$ in the jet $c_{Ao} = 34$ mol/m^3, $\alpha = 1.0$); (d) rounded-shaped crystals ($BaCl_2$ in the jet $c_{Ao} = 34$ mol/m^3, $\alpha = 3.0$); (e) rounded-shaped crystals (Na_2SO_4 in the jet $c_{Ao} = 34$ mol/m^3, $\alpha = 3.0$); (f) rounded-shaped crystals ($BaCl_2$ in the jet $c_{Ao} = 341$ mol/m^3, $\alpha = 0.1$).

reaction equal to 1 (that is, reaction stoichiometry), whereas for larger values of α the reactant fed in the annular region is in excess. Because the concentration of the reactant fed in the nozzle is kept constant for each series, when α is increased the local reactant concentrations increase, but after complete reaction the final solid concentration is constant. At low values of α, nucleation and growth are quite slow; after sampling, crystals continue to grow and crystal morphology is typical for well-formed crystals (see Figure 4a). Increasing α up to 1.0, growth becomes diffusion-controlled, and in fact crystals are dendritics (see Figure 4b and 4c). Notice that in this condition crystals are stable after one minute, meaning that precipitate does not show any further growth. Moreover, when α is in the range between 0.01 and 1.0, an increase in this parameter causes an increase in the final mean crystal size after 30 min, whereas for values of α greater than 1, the mean crystal size decreases after 30 min. This is due to the fact that, given the same final solid concentration after complete reaction, for low concentrations an increase in α favors growth with respect to nucleation, whereas at higher concentrations nucleation moves into the homogeneous region, and an increase in α has the opposite effect. For the highest value ($\alpha = 3$) the mean crystal size is the smallest, but crystals are not stable and the mean crystal size is slowly increasing. Since in this condition the reaction is very fast and, due to homogeneous nucleation, the total particle number density is very high, this further size increase can be attributed to aggregation. Crystal morphology is substantially different (see Figure 4d), and seems to be caused by aggregation and subsequent recrystallization. Figure 5 gives the CSDs for three values of α at the reactor outlet and after 30 min. As we can see, for $\alpha = 0.1$ and 1.5 CSDs are monomodal both at the reactor outlet and after 30 min, whereas for $\alpha = 3$ the CSD presents more peaks. In this last case, both CSD and crystal morphology indicate aggregation.

Figure 6 shows the crystal size evolution with time for case 2 (Na_2SO_4 in the nozzle). The results present some similarities and some differences to the previous case. For low α values, the reaction is not complete, but in this case the maximum of the mean crystal size no longer occurs at $\alpha = 1$, but at $\alpha = 0.01$. These results seem to indicate that the transition to homogeneous nucleation occurs at lower concentrations and that a modification in the nucleation mechanism might occur. If α is increased, the mean crystal size decreases and then increases again, but small differences are detected for higher values of α. However, except for $\alpha = 0.01$, the mean crystal size is more stable after sampling in all the other cases. In Figure 7 the CSDs for different α are reported, and it is possible to see that CSDs at the reactor outlet are more similar after 30 min. Moreover, in case 2 the final mean crystal size after 30 min was generally always lower than in case 1. This can be caused by an enhanced nucleation rate and it can be explained in terms of ion adsorption.

Suspended particles interact depending on the balance between attractive and repulsive forces. Attractive forces are caused by short-range van der Waals interactions, whereas repulsive forces are caused by double-layer repulsions. The electrical double layer is due to the fact that particles have a surface charge, and because dispersions are electrically neu-

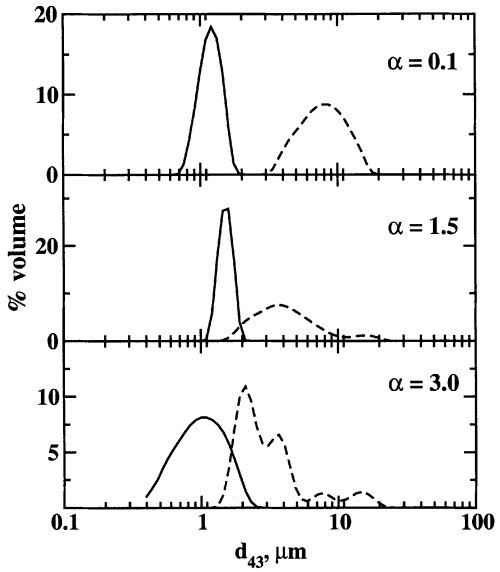

Figure 5. CSDs for several values of α in case 1 at the reactor outlet (solid lines) and after 30 min of gentle stirring (dashed lines).

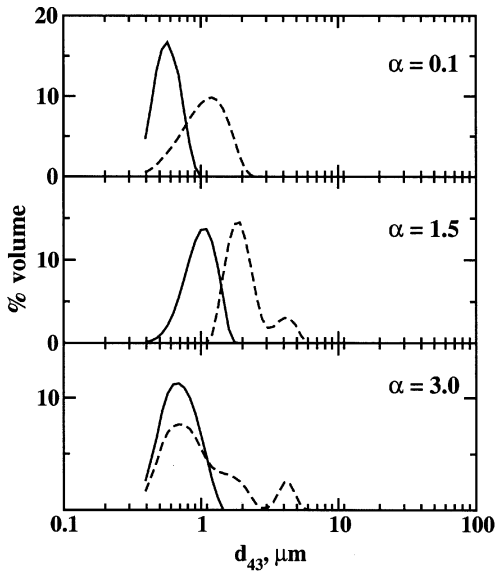

Figure 7. CSDs for several values of α in case 2 at the reactor outlet (solid lines) and after 30 min of gentle stirring (dashed lines).

tral, this charge must be balanced by an opposite charge in the solution. Several mechanisms determine the origin and distribution of the particle charge, and in the case of barium sulfate precipitation, the preferred adsorption of the excess ion seems to be the most important. A useful indication of the dispersion stability is given by the value of the point of zero charge (PZC), which is the ion concentration at which the surface charge is zero. When the surface charge is null, crystals have a greater tendency to aggregate when the system is unstable. For barium sulfate this value is 6.7 in terms of pBa, and since

$$pk_s = p\mathrm{Ba} + p\mathrm{SO}_4 = 10 \tag{34}$$

this is the case when there is an excess of sulfate ion (case 1). It can be inferred that in this case, due to high local values of total particle number density and strong instability in the early stages of nucleation, nuclei tend to aggregate, which results in a reduced nucleation rate. In case 2, nuclei are more stable, and once formed grow, producing crystals; in this case, crystal morphology for $\alpha = 3$ is reported in Figure 4e. As we can see, the structure is very similar to that obtained with the same α in case 1. However, aggregates seem to be constituted of fewer particles, which proves the reduced tendency to aggregate.

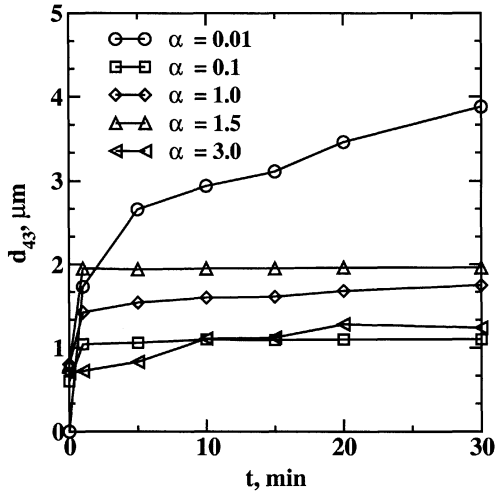

Figure 6. Time evolution of mean crystal size (d_{43}) in sampled suspensions as a function of the concentration ratio (α).

Na_2SO_4 fed in the nozzle, $c_{Ao} = 34$ mol/m^3. The first point represents the tubular reactor outlet.

Results of experiments at a high concentration (case 3) are reported in Figure 8. As we can see, except for $\alpha = 0.01$, in this case the reaction was always complete at the reactor outlet. After sampling, crystals were found to be quite stable, although some small changes in the CSDs were detected. As can be seen in Figure 9, the CSDs maintain the same shape for all the values of α, although generally the first peak decreases and the second one (or ones) increases. This could be considered an indication of the strong tendency of the precipitate to aggregate also for a longer time (30 min), although other factors also might have an influence (such as Otswald ripening). It should be mentioned that in this case CSDs had more than one peak also at the reactor outlet meaning that aggregation began inside the reactor, in spite of the short residence time.

Figure 4f shows the crystal morphology for $\alpha = 0.1$. As can be seen, crystals are spherical aggregates formed by spherical monomers. Formation of these round-shaped crystals has been obtained in the past only by using additives. Results from these studies are very interesting, and can be useful in understanding the role of ion excess on crystal growth. For

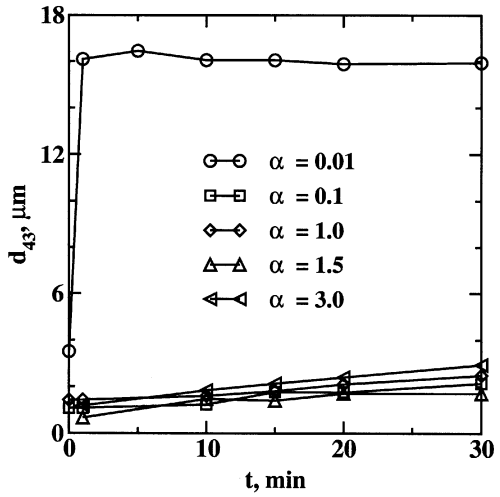

Figure 8. Time evolution of mean crystal size (d_{43}) in sampled suspensions as a function of the concentration ratio (α).

$BaCl_2$ fed in the nozzle, $c_{Ao} = 341$ mol/m^3. The first point represents the tubular reactor outlet.

example, Archibald et al. (1997) studied the effect of additives on barium sulfate morphology, finding that the presence of an additive can favor or discourage the growth of some specific crystal faces. Besides stable faces, they also found some rounded faces composed of a variety of facets creating corrugated sizes that approached ionic dimensions. In their study they inferred that the degree of supersaturation and the ionic strength of the solution play an important role in determining the presence of charged domains on the crystal surface, which may help explain the rapid growth of these

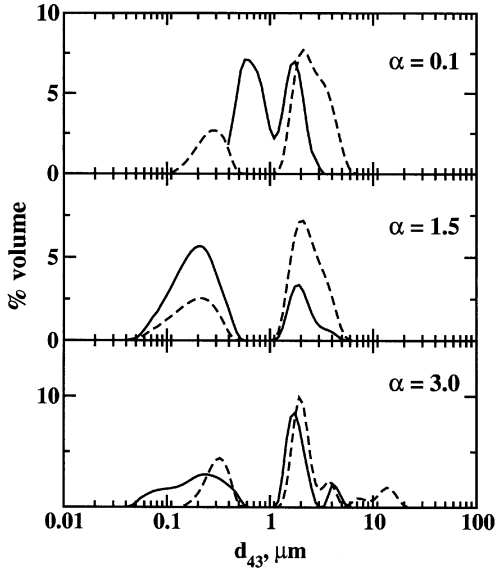

Figure 9. CSDs for several values of α in case 3 at the reactor outlet (solid lines) and after 30 min of gentle stirring (dashed lines).

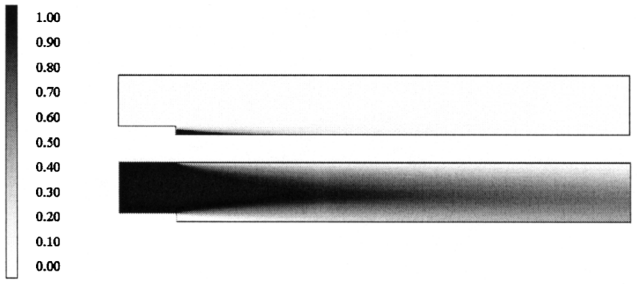

Figure 10. p_1 (top) and p_2 (bottom) near injection and mixing.

rounded faces. Yokota et al. (2000) also investigated the formation and the structure of round-shaped crystals of barium sulfate in the presence of additives. Their main conclusion is that additive ions may adsorb onto particular faces of a crystal and retard the growth of these faces, while other surfaces are not affected.

Comparison with the model

In Figure 10, plots of p_1 (top) and p_2 (bottom) are shown: $p_1 = 1$ in one inlet stream and $p_2 = 1$ in the other, and as soon as the two streams mix together, modes 1 and 2 start to disappear, and then p_1 and p_2 go to zero, whereas p_3 becomes equal to one. Micromixing influences the reaction in zones of the computational domain where p_3 is lower than unity, resulting in local concentrations that are different from weighted concentrations. The mixture fraction variance is greater than zero when p_1 and p_2 or p_3 are not equal to unity, and it is generated by mean local gradients (that is, the mixing zone between the two streams), and dissipated by molecular mixing, whose rate is proportional to ϵ/k and to the constant C_ϕ. The effect of this constant was studied by Piton et al. (2000), and in this work was kept equal to unity.

We considered k_d constant as discussed before. Different shape factors were used; for simulations at low concentration (cases 1 and 2), an average value was used ($k_v = 5$, $k_a = 30$, $\phi_c = 3$), as the differences between various cases were very small (as estimated from the analysis of the SEM photos), and in order to make the code predictive. At high concentrations (case 3) crystals were considered as spheres ($k_v = \pi/6$, $k_a = \pi$, $\phi_c = 1$). Notice that this model is perfectly symmetric; in fact, it is not able to distinguish between barium excess and sulfate excess.

Model predictions at the reactor outlet (averaged value along the radial direction) are presented in Figure 11. In the top of the figure the mean crystal size predicted by the model is compared with experimental data, and as mentioned before, the model is not able to give different predictions for case 1 and 2. However, both experimental data and model predictions show a shallow maximum for $\alpha = 1.5$.

The total particle number density is presented in the bottom of Figure 11. Experimental data at the reactor outlet are not available for this variable, but the total number density of crystals formed when the reaction is complete at $t = 30$ min, can be derived from CSDs measured. In fact, knowledge of

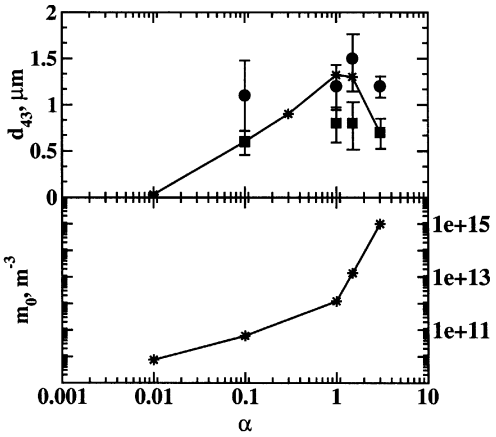

Figure 11. Top, mean crystal size vs. α (error bars, two standard deviations determined based on 5–6 runs); bottom, total particle number density vs. α.

Circles, experimental data in case 1; squares, experimental data in case 2; solid line with stars, model predictions.

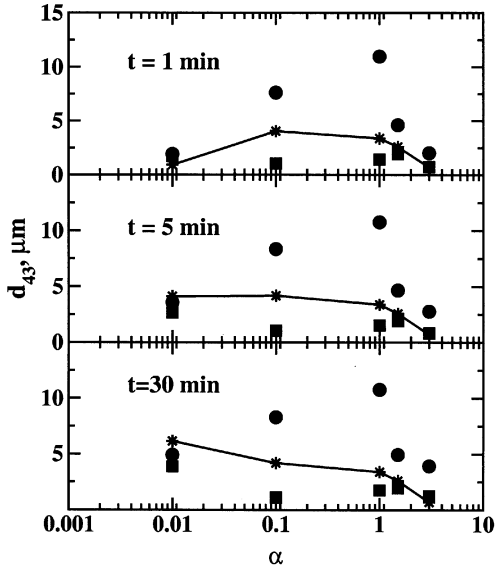

Figure 13. Mean crystal size vs. α at different instants.

Circle, experimental data in case 1; square, experimental data in case 2; solid line with stars, model predictions.

the CSD and the final solid concentration are enough to determine the final total particle number density. Also, these experimental data can be compared with model predictions by extending the precipitation model to the second part of the experiment. Assuming that mixing is important only in the first part, by using a simple well-mixed approach, it is possible to model the reaction course until it is complete.

In Figure 12 results from case 1 and 2 are compared with model predictions. As it is possible to observe, experimental data are very dispersed. This is because this property is not directly measured but is derived from the CSD, and any uncertainty is amplified by the third power; in addition, very small particles are not measured by the particle-size analyzer. Also for this property a big difference between case 1 and 2 was observed, and model predictions are closer to case 2. The simulation results confirm that the reaction is not complete at low values of α, but the nucleation step is also ongoing (compare m_0 at $\alpha = 0.01$ in Figures 11 and 12).

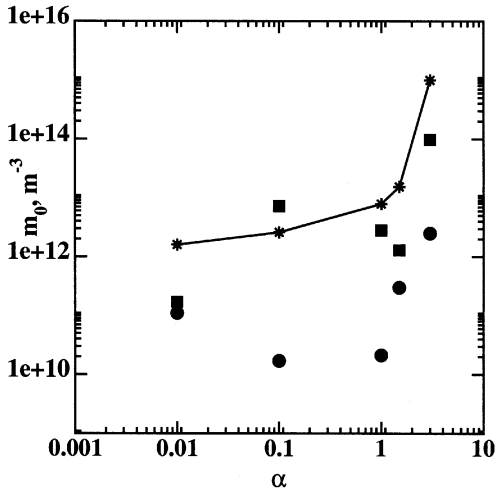

Figure 12. Total particle number density vs. α for $t = 30$ min (complete reaction).

Circle, number density derived from experimental data in case 1; square, number density derived from experimental data in case 2; solid line with stars, model predictions.

Moreover, model predictions can be compared with the experimental mean crystal size obtained at different times in the second part of the experiment. This comparison is very interesting, since given the fixed concentration of the limiting reactant, and, thus, of the maximum final solid concentration, when the reaction is not complete, particles might have similar sizes and assume different sizes only when the reaction proceeds. This comparison is made in Figure 13. As mentioned before, the mean crystal size in case 2 is always lower than in case 1, and model predictions are between the two series of experimental data, but are closer to case 2.

The results presented in Figures 12 and 13 clearly show that the kinetic expressions used in this work are able to give good agreement in terms of the order of magnitude; however, a lack of information concerning this nonsymmetric effect of the ion excess still exists. Moreover, a comparison of the model predictions with and without the micromixing model showed that in these operating conditions micromixing has a small effect, and then macro- and mesomixing play a major role in determining the final CSD.

In Figure 14 model predictions at the reactor outlet are compared with experimental data in case 3. In the top of the figure, the mean crystal size is compared with the model with and without aggregation. In this case experiments were found to be much more reproducible (the standard deviation was as low as 2–5%), and for this reason only the first experiments were replicated 4–5 times, whereas the last ones were replicated only twice. As was said before, here we consider only aggregation with constant kernel (Eq. 27). The comparison shows that in these operating conditions if aggregation is ne-

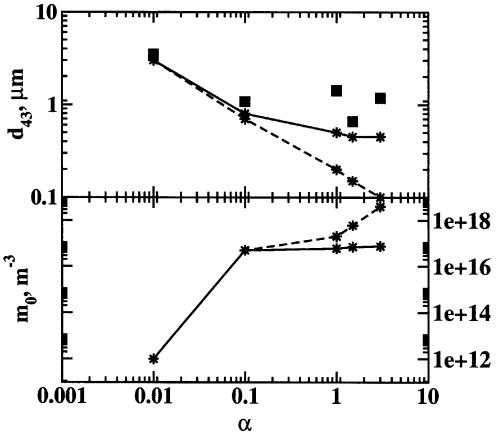

Figure 14. Top, mean crystal size vs. α; bottom, total number density vs. α.

Squares, experimental data in case 3; solid line with stars, model predictions; dashed line with stars, model predictions neglecting aggregation.

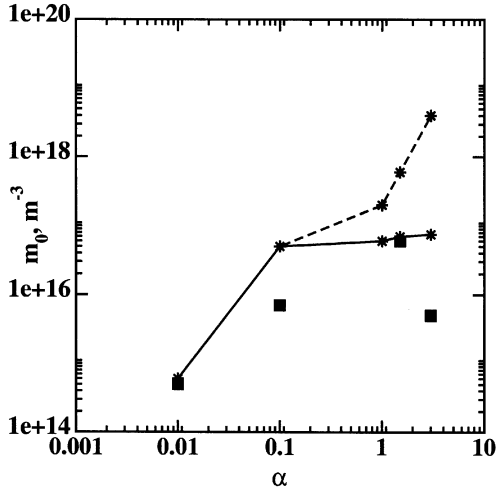

Figure 15. Total particle number density vs. α for $t = 30$ min (complete reaction).

Square, number density derived from experimental data in case 3; solid line with stars, model predictions; dashed line with stars, model predictions neglecting aggregation.

glected, the mean crystal size is sensibly underestimated, for α greater than 0.1. It is useful to compare the mean crystal size predicted by the model without aggregation and the CSDs presented in Figure 9. From this analysis it is possible to observe that the model is able to predict the size of the monomers, but only when aggregation is included, the model is able to predict the size of the agglomerates. However the mean size of agglomerates is still higher than model predictions. This could be caused by the fact that turbulent aggregation is not considered. In fact, it has been shown that turbulent aggregation might be important for particles smaller than the Kolmogorov scale (Tontrup et al., 2000). Useful pieces of information can be obtained by evaluating the Peclet number, which is an estimate of the ratio between shear-induced and Brownian coagulation rate, and is defined as

$$Pe = \frac{3\pi\mu L_{43}^3 \gamma_l}{k_B T} \tag{35}$$

where μ is the fluid viscosity and

$$\gamma_l = \sqrt{\frac{2\epsilon}{15\nu}} \tag{36}$$

When $Pe < 0.001$, only Brownian aggregation can be considered, whereas the Brownian contribution is negligible when $Pe > 10$. Depending on the mean crystal size, Pe assumes different values, and for example, when L_{43} falls in the range between 10^{-7} m and 10^{-6} m, Pe is approximately included in the range 0.001–100, which means that both contributions should be taken into account. However, this can be done only if a more accurate approach for the population balance is used.

The total particle number density is reported in the bottom of Figure 14. Model predictions without aggregation show an increase in m_0 increasing concentration, whereas, when aggregation is included, the final m_0 is reduced by particle–particle interactions. Also in this case, the total particle number density derived from experimental CSD for $t =$ 30 min is compared with model predictions with and without aggregation (see Figure 15); again nucleation is still ongoing at the reactor outlet for $\alpha = 0.01$ (compare Figures 14 and 15). Notwithstanding the dispersion of the experimental data, it is interesting to notice that the effect of aggregation is to reduce m_0, which results in a better agreement.

Unlike cases 1 and 2, in these operating conditions, micromixing is also very important; in fact, due to high reactant concentrations, precipitation is very fast and is confined to a small region near the injection where p_3 is lower than one. As a matter of fact, in case 3 neglecting micromixing causes an error of 30–50% on the mean crystal size and of 150–200% on the total particle number density.

Conclusion

Turbulent precipitation of barium sulfate in a tubular reactor has been studied in a wide variety of operating conditions. A commercial CFD code was coupled with a subgrid-scale micromixing model (FM-PDF) and with the SMM for the population balance.

Experimental results show that ion excess strongly influences the final CSD, which can be explained in terms of the preferential absorption of the excess ion, whereas the role of the activity coefficients seems to be in doubt (Marchisio et al., 2001b). This finding is in agreement with other works (Aoun et al., 1996; Wong et al., 2001), and this shows the need for a systematic kinetic study on the effect of ion excess on nucleation and growth rate, in a wider concentration range.

Moreover, it has been shown that when concentration is increased, aggregation and growth from the solution take place simultaneously. This causes the formation of very stable aggregates that can be defined as agglomerates. In general, comparison with model predictions shows good agreement. The role of the micromixing model has been shown to be critical, especially for higher concentrations.

Moreover, turbulent aggregation should be taken into account in the case of a high aggregation rate. This involves the use of nonconstant kernels that can be handled by using more sophisticated population balance treatments (that is, DPB or QMOM).

Acknowledgments

The research was partially supported by an Italian National research project (PRIN-Analisys and modeling of solid–liquid mixing processes). The authors gratefully acknowledge Prof. Rodney O. Fox for the valuable discussions concerning the use of the FM-PDF model, and Prof. Marco Vanni for his help in the computational work and the useful discussions on aggregation kinetics.

Literature Cited

Aoun, M., E. Plasari, R. David, and J. Villermaux, "Are Barium Sulphate Kinetics Sufficiently Known for Testing Precipitation Reactor Models?," *Chem. Eng. Sci.*, **51**, 2449 (1996).

Aoun, M., E. Plasari, R. David, and J. Villermaux, "A Simultaneous Determination of Nucleation and Growth Rates from Batch Spontaneous Precipitation," *Chem. Eng. Sci.*, **54**, 1161 (1999).

Archibald, D. D., B. P. Gaber, J. D. Hopwood, S. Mann, and T. Boland, "Atomic Force Microscopy of Synthetic Barite Microcrystals," *J. Crystal Growth*, **172**, 231 (1997).

Armenante, P. M., and D. J. Kirwan, "Mass Transfer Coefficient to Microparticles in Agitated Systems," *Chem. Eng. Sci.*, **44**, 2781 (1989).

Baldyga, J., and W. Orciuch, "Closure Problem for Precipitation," *Chem. Eng. Res. Des.*, **75A**, 160 (1997).

Baldyga, J., W. Podgorska, and R. Pohorecki, "Mixing-Precipitation Model with Application to Double Feed Semibatch Precipitation," *Chem. Eng. Sci.*, **50**, 1281 (1995).

Bramley, A. S., M. J. Hounslow, R. Newman, W. R. Paterson, and C. Pogessi, "The Role of Solution Composition on Aggregation During Precipitation Agglomeration of Yttrium Oxalate," *Chem. Eng. Res. Des.*, **75A**, 119 (1997).

Bromley, L. A., "Thermodynamic Properties of Strong Electrolytes Aqueous Solutions," *AIChE J.*, **19**, 313 (1973).

Dirksen, J. A., and T. A Ring, "Fundamentals of Crystallization: Kinetic Effects on Particle Size Distributions and Morphology," *Chem. Eng. Sci.*, **46**, 2389 (1991).

Fox, R. O., "On the Relationship Between Lagrangian Micromixing Models and Computational Fluid Dynamics," *Chem. Eng. Process.*, **37**, 521 (1998).

Hounslow, M. J., R. L. Ryall, and V. R. Marshall, "A Discretized Population Balance for Nucleation, Growth, and Aggregation," *AIChE J.*, **34**, 1821 (1988).

Li, K. T., and H. L. Toor, "Turbulent Reacting Mixing with a Series-Parallel Reaction: Effect of Mixing on Yield," *AIChE J.*, **32**, 1312 (1986).

Litster, J. D., D. J. Smit, and M. J. Hounslow, "Adjustable Discretized Population Balance for Growth and Aggregation," *AIChE J.*, **41**, 591 (1995).

Marchisio, D. L., R. O. Fox, A. A. Barresi, and G. Baldi, "A CFD Approach to Study the Local Importance of Aggregation in Precipitation," *Proc. Int. Conf. on Multiphase Flow in Industrial Plants*, Bologna, Italy, p. 363 (2000).

Marchisio, D. L., "Precipitation in Turbulent Fluids," PhD Diss., Politecnico di Torino, Torino, Italy (2002).

Marchisio, D. L., A. A. Barresi, and R. O. Fox, "Simulation of Turbulent Precipitation in a Semibatch Taylor-Couette Reactor Using CFD," *AIChE J.*, **47**, 664 (2001a).

Marchisio, D. L., R. O. Fox, A. A. Barresi, M. Garbero, and G. Baldi, "On the Simulation of Turbulent Precipitation in a Tubular Reactor via Computational Fluid Dynamics," *Chem. Eng. Res. Dev.*, **79A** (2001b).

Marchisio, D. L., R. O. Fox, A. A. Barresi, and G. Baldi, "On the Comparison Between Presumed and Full PDF Methods for Turbulent Precipitation," *Ind. Eng. Chem. Res.*, **40**, 5132 (2001c).

McGraw, R., "Description of Aerosol Dynamics by the Quadrature Method of Moments," *Aerosol Sci. Technol.*, **27**, 255 (1997).

Nagata, S., *Mixing-Principles and Applications*, Chap. 6, Kodansha, Tokyo, p. 268 (1975).

Nielsen, A. E., *Kinetics of Precipitation*, Pergamon Press, London (1964).

Nielsen, A. E., "Electrolyte Crystal Growth Mechanisms," *J. Crystal Growth*, **67**, 289 (1984).

Nielsen, A. E., and J. M. Toft, "Electrolyte Crystal Growth Kinetics," *J. Crystal Growth*, **67**, 278 (1984).

Pagliolico, S., D. Marchisio, and A. A. Barresi, "Influence of Operating Conditions on $BaSO_4$ Crystal Size and Morphology in a Continuous Couette Precipitator," *J. Therm. Anal. Cal.*, **56**, 1423 (1999).

Phillips, R., S. Rohani, and J. Baldyga, "Micromixing in a Single-Feed Semi-Batch Precipitation Process," *AIChE J.*, **45**, 82 (1999).

Pipino, M., and R. O. Fox, "Reactive Mixing in a Tubular Jet Reactor: A Comparison of PDF Simulations with Experimental Data," *Chem. Eng. Sci.*, **49**, 5229 (1994).

Piton, D., R. O. Fox, and B. Marcant, "Simulation of Fine Particles Formation by Precipitation Using Computational Fluid Dynamics," *Can. J. Chem. Eng.*, **78**, 983 (2000).

Randolph, A. D., and M. A. Larson, *Theory of Particulate Processes*, 2nd ed., Academic Press, San Diego (1988).

Saffman, P. G., and J. S. Turner, "On the Collision of Drops in Turbulent Clouds," *J. Fluid Mech.*, **1**, 16 (1956).

Smoluchowksy, M. Z., "Versuch Einer Methematischen Theorie der Koagulationskinetic Kolloider Losunger," *Z. Phys. Chem.*, **92**, 129 (1917).

Sung, M. H., I. S. Choi, J. S. Kim, and W. S. Kim, "Agglomeration of Yttrium Oxalate Particles Produced by Reaction Precipitation in a Semi-Batch Reactor," *Chem. Eng. Sci.*, **55**, 2173 (2000).

Tontrup, C., F. Gruy, and M. Cournil, "Turbulent Aggregation of Titania in Water," *J. Colloid Interface Sci.*, **229**, 511 (2000).

Wei, H., and J. Garside, "Application of CFD Modelling to Precipitation Systems," *Chem. Eng. Res. Des.*, **70A**, 219 (1997).

Wong, D. C. Y., Z. Jaworski, and A. W. Nienow, "Effect of Ion Excess on Particle Size and Morphology During Barium Sulphate Precipitation: an Experimental Study," *Chem. Eng. Sci.*, **56**, 1 (2001).

Yokota, M., E. Oikawa, J. Yamanaka, A. Sato, and N. Kubota, "Formation and Structure of Rounded-Shaped Crystals of Barium Sulfate," *Chem. Eng. Sci.*, **55**, 4379 (2000).

Zauner, R., and A. G. Jones, "Determination of Nucleation, Growth, Agglomeration and Disruption Kinetics from Experimental Data: The Calcium Oxalate System," *Chem. Eng. Sci.*, **55**, 1 (2000).

Manuscript received June 6, 2001, and revision received Feb. 12, 2002.